JACS
JOURNAL OF THE AMERICAN CHEMICAL SOCIETY
pubs.acs.org/JACS

Article

Bottlebrush Polymers with Sequence-Controlled Backbones for Enhanced Oligonucleotide Delivery

Yun Wei,[‖] Peiru Chen,[‖] Mengqi Ren,[‖] Deng Li, Jiachen Lin, Tingyu Sun, Yuyan Wang, Shaobo Yang, Christopher Nenopoulos, Christopher Oetheimer, Yao Li, Chenyang Xue, Mona Minkara, and Ke Zhang*

Cite This: J. Am. Chem. Soc. 2024, 146, 34763−34770

Read Online

ACCESS | Metrics & More | Article Recommendations | Supporting Information

ABSTRACT: The clinical translation of oligonucleotide-based therapeutics continues to encounter challenges in delivery. In this study, we introduce a novel class of delivery vehicles for oligonucleotides that are based on poly(ethylene glycol) (PEG) bottlebrush polymers with sequence-defined backbones. Using solid-phase synthesis and bespoke phosphoramidites, the oligonucleotide and the polymer backbone can be assembled on the solid support. The synthesis allows chemical modifiers such as carbon 18 (C_{18}) units to be incorporated into the backbone in specific patterns to modulate the cell−material interactions. Subsequently, PEG side chains were grafted onto the polymer segment of the resulting polymer−oligonucleotide conjugate, yielding bottlebrush polymers. We report an optimal pattern of the C_{18} modifier that leads to improved cellular uptake, plasma pharmacokinetics, biodistribution, and antisense activity *in vivo*. Our results provide valuable insights into the structure−property relationship of polymer−oligonucleotide conjugates and suggest the possibility of tuning the polymer backbone to meet the specific delivery requirements of various diseases.

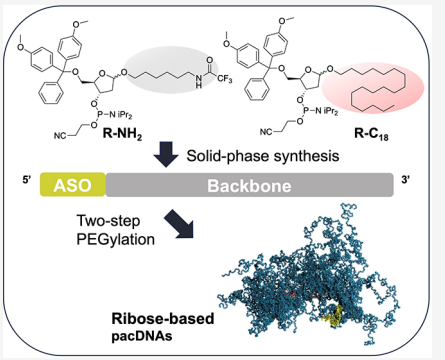

INTRODUCTION

Oligonucleotide-based therapeutics hold immense promise for treating diseases through diverse mechanisms, such as gene regulation, receptor binding, and alternative splicing, among others.[1,2] However, clinical development of oligonucleotide drug candidates often faces setbacks attributed to poor target engagement *in vivo* due to limited uptake by target organs and cells, limiting their use to a few concentrated disease settings.[3−5] Current strategies to improve drug potency generally focus on chemical modifications, bioconjugation with antibodies, peptides, or small molecule ligands, and polyplex carriers such as lipid nanoparticles and cationic polymers.[6−9] However, concerns remain regarding potential toxicity and immunogenicity associated with chemical modifications and carriers, as well as suboptimal biodistribution following systemic administration.[10] Thus, the development of a delivery system that can simultaneously enhance nuclease stability, facilitate rapid intracellular delivery of oligonucleotides, and ensure sufficient distribution into target tissues holds the potential to bridge the critical development gap.[9−11]

Previously, we have reported the design of a bottlebrush polymer−oligonucleotide conjugate (termed pacDNA: polymer-augmented conjugate of DNA), which effectively mitigates protein−oligonucleotide interactions while maintaining unaffected target RNA binding.[12,13] This unique selectivity is achieved through the more densely packed poly(ethylene glycol) (PEG) side chains compared to typical linear or slightly branched PEG, which leads to reduced protein binding and consequently, fewer side effects *in vivo* that derive from unwanted protein−oligonucleotide interactions.[14] Additionally, the large size of the conjugate reduces renal clearance and enhances circulation in the bloodstream, leading to significantly increased biodistribution to nonliver/kidney organs including difficult-to-target sites such as the skin, skeletal muscle, and heart.[15,16]

The bottlebrush polymer in our earlier system was prepared by ring-opening metathesis polymerization of norbornenyl monomers using a Grubbs third-generation catalyst. We identified three aspects where this system can be improved: (1) batch-to-batch consistency, (2) residue heavy metal content, and (3) control over the bottlebrush polymer backbone. Herein, we report the design, synthesis, and biological testing of a novel deoxyribose 3′−5′ phosphodiester-derived bottlebrush−oligonucleotide conjugate, which offers unprecedented flexibility and control in the backbone chemistry, length, sequence, and composition. We demonstrate

Received: September 23, 2024
Revised: November 7, 2024
Accepted: November 13, 2024
Published: November 27, 2024

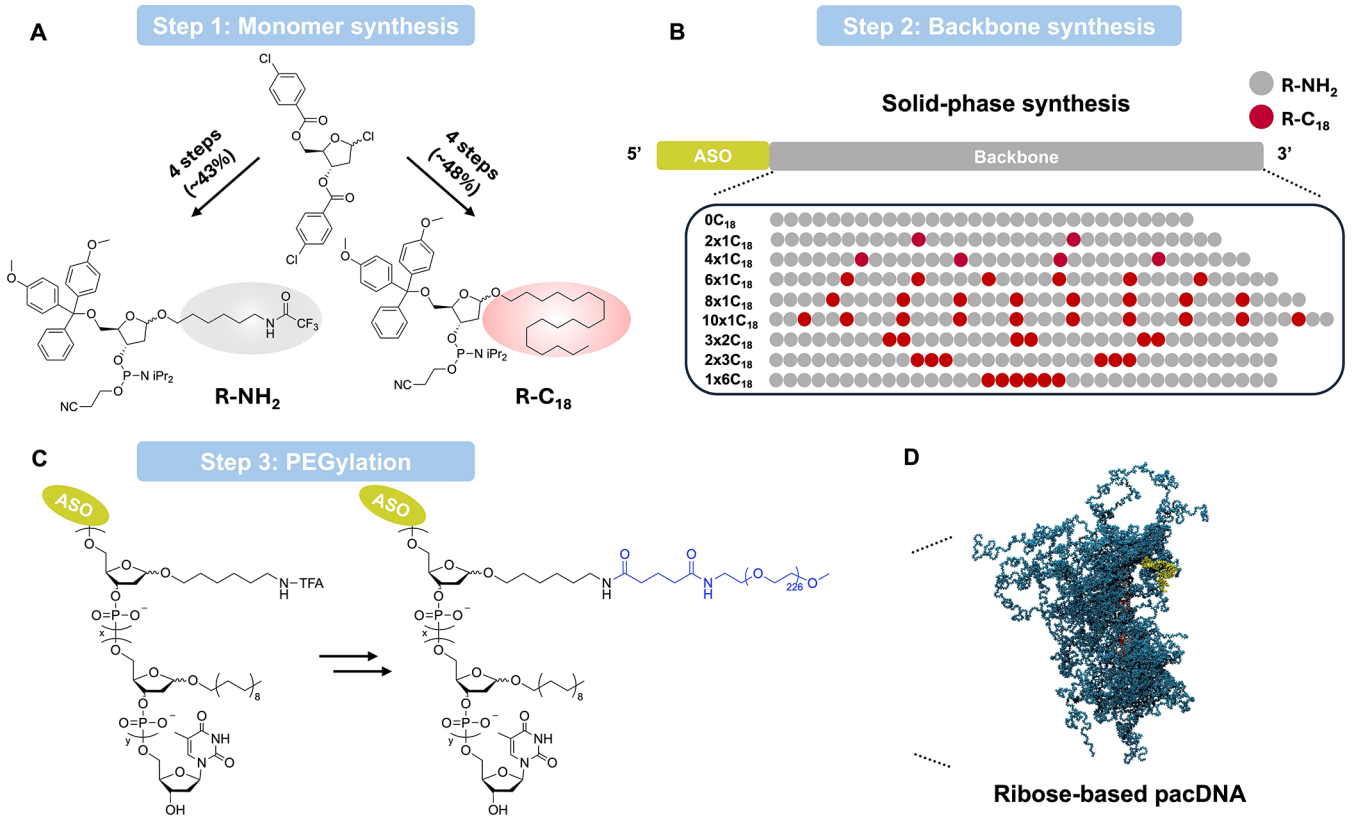

Figure 1. Design of ribose-based pacDNAs. (A,B) Synthetic scheme and backbone designs of pacDNAs. The gray and red circle represents the R-NH_2 unit and R-C_{18} unit, respectively. ASO: antisense oligonucleotide. (C) Schematics of the PEGylation process of ribose-based pacDNA. (D) Molecular dynamics (MD) simulation of ribose-based pacDNA with four C_{18} modifiers (cyan: PEG; gray: backbone; red: C_{18}; yellow: ASO).

an optimized backbone structure containing patterned C_{18} units for application in targeting Kirsten Rat Sarcoma Virus (KRAS) mRNA in a mouse allograft model. These findings provide valuable insights for the development of tailored vehicles to meet indication-specific delivery requirements.

RESULTS AND DISCUSSION

The poly(2-deoxyribose phosphodiester) backbone polymer is constructed using a stepwise condensation approach, employing two bespoke modified phosphoramidites: ribose NH_2 (R-NH_2) and ribose C_{18} (R-C_{18}). The modifiers were synthesized from 1-chloro-3,5-di(4-chlorbenzoyl)-2-deoxy-D-ribose in ~40% overall yields in multigram scales (Figures 1A and S10−S25; Schemes S1 and S2). The oligonucleotide component was synthesized as an integral part of the backbone of the solid support.

Due to the utilization of the same phosphoramidite chemistry, the oligonucleotide can be positioned at either the 3′ or the 5′ of the polymer backbone without requiring additional postconjugation steps. For the purposes of this proof-of-concept study, antisense oligonucleotides (ASOs) targeting the 3′ untranslated region (UTR) of both human and mouse KRAS mRNA (ASO1 and ASO2, respectively) were selected as the payload for this ribose-based pacDNA, which were positioned at the 5′ of the ribose backbone (Figure 1B).[17,18] The backbone is designed to incorporate 30 repeating units of ribose NH_2, which can be subsequently PEGylated to give the bottlebrush morphology (Figure 1C,D).[16,19] Because the phosphodiester ribose backbone is significantly more hydrophilic than the polynorbornene (PN)-based pacDNA, which may limit material−cell membrane interactions, leading to reduced cell uptake, we investigated how hydrophobic C_{18} modifiers introduced into the backbone can affect the cellular uptake and biodistribution *in vivo*. We varied the numbers of C_{18} modifiers (ranging from 0 to 10) as well as their distribution patterns (for backbones containing six C_{18} modifiers) in order to probe the structure−property relationship (Figure 1B).

Following the completion of solid-phase backbone/ASO synthesis, the trifluoroacetyl protecting groups were removed, and the hybrid strand was cleaved from the solid support. The successful strand was isolated using a dimethoxytrityl (DMT)-affinity column. To construct the bottlebrush structure, the amine groups on the backbone were derivatized with a heterodifunctional *N*-hydroxysuccinimide (NHS)- and methyl-terminated 10 kDa PEG, using a two-stage process.[19] The purified strand was PEGylated initially in 1× phosphate buffered saline (PBS) at 4 °C overnight. The partially PEGylated product was desalted, lyophilized, and subsequently reacted with another equivalent of PEG in anhydrous *N*,*N*-dimethylformamide (DMF) for full derivatization. Excess PEG and residues were removed by aqueous gel permeation chromatography (GPC), yielding highly uniform, narrowly dispersed pacDNA structures, as evidenced by aqueous and DMF GPC (Figure 2A; Table S2), dynamic light scattering (DLS) (Figures 2B and S1), and transmission electron microscopy (TEM) (Figure 2C). The uniformity of pacDNA particles was consistently observed across all samples irrespective of the quantity or arrangement of R-C_{18} units, suggesting that the C_{18} modifiers do not cause aggregation in

https://doi.org/10.1021/jacs.4c13285
J. Am. Chem. Soc. 2024, 146, 34763−34770

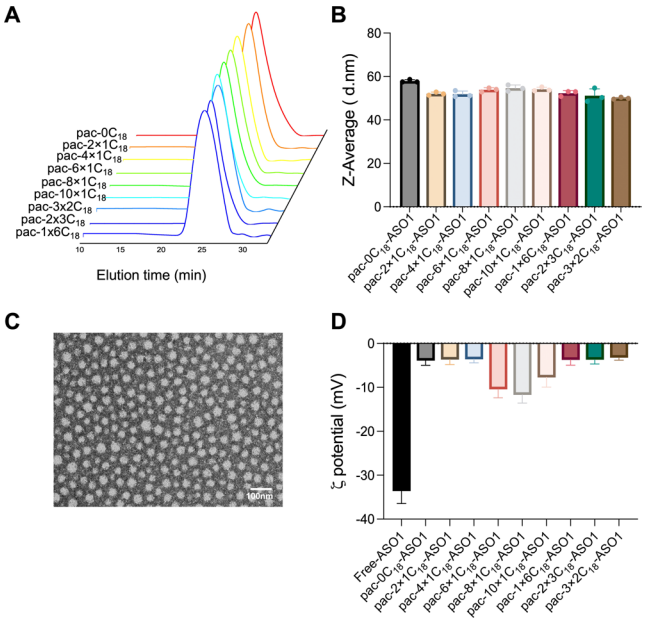

Figure 2. Characterization of ribose-based pacDNAs. (A) Aqueous GPC chromatograms of pacDNAs after two-stage PEGylation. (B) pacDNA Z-average (the intensity-weighted mean) molecular size in Nanopure water as determined by DLS. (C) Representative TEM image of pacDNA (pac-4 × $1C_{18}$-ASO1) with negative staining using 2% uranyl acetate. (D) pacDNA ζ potential in Nanopure water.

solution. ζ potential measurement revealed that all pacDNA samples are slightly anionic (−3.26 to −11.71 mV) in Nanopure water compared with free oligonucleotides (−33.6 mV) (Figure 2D). Collectively, these results demonstrate that ribose-based pacDNAs can be robustly synthesized, allowing for fine-tuning of the size/backbone sequence of the pacDNAs and the potential to modulate their bioactivities. A comparison between ribose- and PN-based pacDNAs can be found in Figure S2.

Next, we assessed the intracellular delivery efficacy of the pacDNA panel in NCI-H358 cells, a nonsmall lung carcinoma line harboring $KRAS^{G12C}$ mutation. Flow cytometry analysis revealed that as the number of R-C_{18} units increased within the bottlebrush backbone, cellular uptake also increased (Figure 3A), suggesting the structurally more hydrophobic pacDNA constructs may exhibit stronger material−cell interactions. The trend does not change when bottlebrush polymers lacking the ASO component were tested (Figure S3A). Interestingly, when the same number of C_{18} units was incorporated into the bottlebrush backbone, the evenly distributed patterns demonstrated higher cellular uptake efficiencies (Figure 3B), while the clustering of C_{18} units reduced cell uptake. In fact, when all six C_{18} units were clustered together (pac-1 × $6C_{18}$-ASO1), the cellular uptake was comparable to that of the pacDNA without any C_{18} units (pac-$0C_{18}$-ASO1). The flow cytometry measurements were further supported by confocal microscopy. Cy5-labeled pacDNAs were incubated with NCI-H358 cells for 8 h before imaging. Again, pacDNAs with a higher number of C_{18} units showed greater cell uptake (Figures 3C and S4). We postulate that when R-C_{18} units are positioned adjacent to one another, the self-interaction among C_{18} decreases their tendency to interact with the cellular membrane. In contrast, separating the C_{18} units spatially reduces such self-interactions, leading to a higher potential energy state and stronger tendency to bind with the cell membrane upon contact. Increased cellular uptake of ASO by lipid conjugation has been reported.[20,21] However, lipid conjugates often exhibit increased cytotoxicity, possibly due to membrane lytic activity of the amphiphilic conjugate.[22,23] In contrast, the pacDNAs do not cause cytotoxicity (Figure S3B) even though they contain multiple C_{18} units. One interpretation is that the sterics of the pacDNA make it difficult for the lipid chains to aggregate and exhibit surfactant-like properties, limiting the potential membrane lytic activity.

To gain molecular level insights, we carried out full atomistic MD simulations to quantitatively assess the energy of interaction between water molecules and pacDNAs with six C_{18} units arranged in different distribution patterns. In this context, interaction energy refers to the total energy arising from all intermolecular forces between the pacDNA molecules and surrounding water molecules. A more negative interaction energy indicates stronger interactions with water, leading to greater solubility of the pacDNA in aqueous environments. We hypothesize that the pacDNA with the least amount of lipid self-interactions will be the most prone to membrane binding. This hypothesis can be tested by measuring pacDNA interaction energy in water—structures with the least interaction energy with water (most difficult to dissolve) should exhibit the highest cell uptake. To make the simulation computationally feasible, all PEG side chains were truncated to 20 mer, which was found to be sufficiently large to inhibit backbone coiling under simulation conditions. The simulation trajectory confirms more extensive lipid−lipid interactions for clustered vs spaced arrangement of C_{18} units (Figure 3D). The pacDNA with the smallest spacing (pac-1 × $6C_{18}$) exhibited the most interaction energy (most negative). This result suggests that when a constant number of C_{18} units are present in the backbone, their clustering increases solubility in water and therefore reduces C_{18} interactions with cell membranes, leading to lower cell uptake (Figure 3E). Conversely, the pacDNA with the largest spacing (pac-6 × $1C_{18}$) exhibited the lowest interaction energy (least negative), indicating that pac-6 × $1C_{18}$ has the least tendency to be dissolved in water, and by extension, an enhanced propensity for interacting with the cell membrane and cellular uptake. These observations underscore the pivotal role of the digital backbone design, which allows for precise tuning of the biophysical behavior of pacDNAs.

Next, we assessed the efficacy of the pacDNAs to engage with cytosolic mRNA targets by using pacDNAs bearing ASO1 (vide supra) and varying numbers of evenly distributed C_{18} units. Western blot analysis showed the downregulation of KRAS protein levels in all pacDNA-treated groups (Figure 3F). Interestingly, when pacDNA has at least two C_{18} units, KRAS depletion levels did not vary significantly. We also analyzed cell viability using a 3-(4,5-dimethylthiazol-2-yl)-2,5 diphenyl tetrazolium bromide (MTT) assay. All pacDNAs significantly inhibited tumor cell growth, with inhibition levels ranging from 40 to 60% compared to nontreated cells, while the free ASO1 showed no inhibitory activity (Figures 3G and S5).

Prior to nominating a candidate for efficacy studies, it is important to understand how the pacDNA backbone series affects plasma pharmacokinetics (PK) and biodistribution. Cy5-labeled pacDNAs were intravenously (i.v.) administered to C57BL/6 mice via the tail vein, and blood plasma samples were collected by submandibular puncture at predetermined time points over a 72 h period. Compared to free ASO, all pacDNA constructs, regardless of the number of R-C_{18} units in the backbone, exhibited significantly prolonged circulation

https://doi.org/10.1021/jacs.4c13285
J. Am. Chem. Soc. 2024, 146, 34763−34770

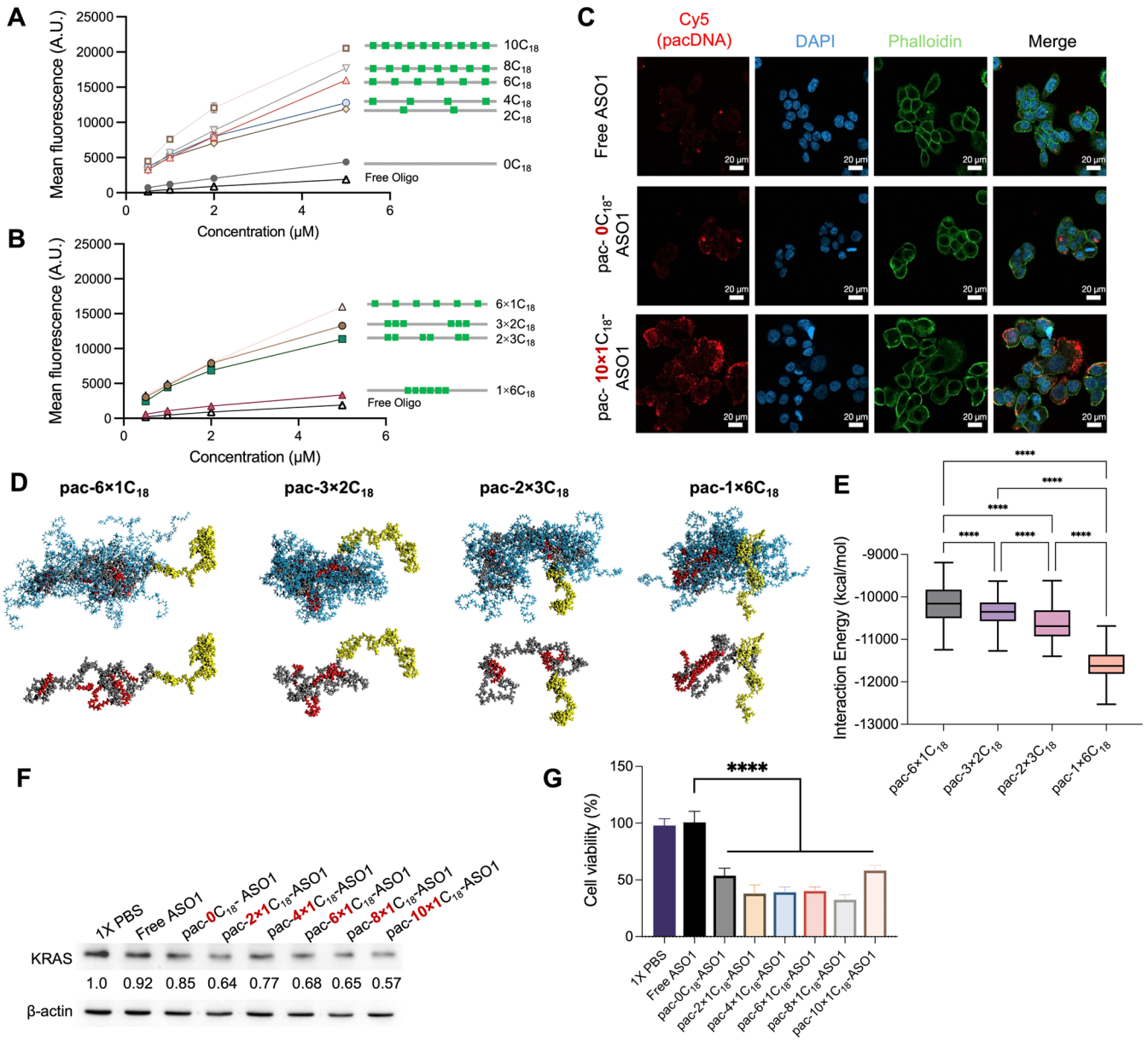

Figure 3. *In vitro* properties of ribose-based pacDNAs. (A,B) Cellular uptake by NCI-H358 cells of Cy5-labeled pacDNAs-ASO1 containing varying numbers and arrangement of C_{18} modifiers after 4 h incubation, as determined by flow cytometry. MFI: mean fluorescence intensity. (C) Confocal microscopy of NCI-H358 cells treated with Cy5-labeled free ASO1 or pacDNAs-ASO1 for 8 h (additional samples: Figure S4). Cy5-labeled ASO (red), DAPI-stained nuclei (blue), and phalloidin-stained F actin (green) are presented separately. (D,E) Interaction energy of pacDNAs after interaction with water as determined by MD simulation and representative molecular snapshots from the simulation trajectory (up row is the structures of entire molecules, down row is the corresponding structures without PEG chains to show backbones more clearly; cyan: PEG; gray: backbone; red: C_{18}; yellow: ASO). (F) KRAS depletion efficiency of 10 μM pacDNAs-ASO1 in NCI-H358 cells. The number shows the relative KRAS protein level analyzed by ImageJ software. (G) Inhibitive effect of 10 μM pacDNAs-ASO1 on the proliferation of NCI-H358 cells after 48 h incubation. Statistical analysis was performed using one-way ANOVA. ****$P < 0.0001$.

times (Figure 4A). Analyzing the plasma PK using a two-compartment model, it can be seen that the distribution half-lives ($t_{1/2\alpha}$) generally decrease with increasing R-C_{18} number (Figure 4B). Interestingly, a straightforward correlation was not observed for the elimination half-life ($t_{1/2\beta}$), which increases first and then decreases with C_{18} numbers, peaking at pac-4 × $1C_{18}$. The insertion of two or four R-C_{18} units may represent optimized structures because these specific arrangements are capable of significantly enhancing the bioavailability of the ASO as characterized by area under the curve (AUC_∞), while being sufficiently strong for cellular uptake.

We next carried out a biodistribution study comparing the different pacDNA constructs using C57BL/6 mice bearing the K273 tumor allograft. The K273 cell is a $KRAS^{G12D}$ lung cancer line derived from a genetically engineered mouse model (GEMM). The pacDNAs were administered i.v., and fluorescence images were captured at predetermined time points (Figure 4C). The fluorescence signal at the tumor site first increases and then decreases with increasing C_{18} numbers, following a similar trend to the plasma elimination half-life. To quantitatively analyze pacDNA biodistribution among major organs and tissues, mice were sacrificed 72 h after injection, and tissue lysates were used to determine distribution as %

https://doi.org/10.1021/jacs.4c13285
J. Am. Chem. Soc. 2024, 146, 34763−34770

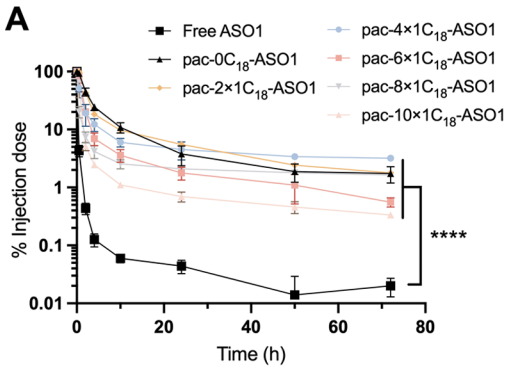

B

Sample ID	$t_{1/2\alpha}$ (h)	$t_{1/2\beta}$ (h)	AUC_{∞}(nmol/mL.h)
Free-ASO1	0.10	0.95	2.61
pac-0C_{18}-ASO1	1.05	6.55	25.55
pac-2×1C_{18}-ASO1	0.95	14.15	25.57
pac-4×1C_{18}-ASO1	0.86	24.25	18.33
pac-6×1C_{18}-ASO1	0.79	10.85	12.19
pac-8×1C_{18}-ASO1	0.66	11.59	5.76
pac-10×1C_{18}-ASO1	0.70	8.73	4.37

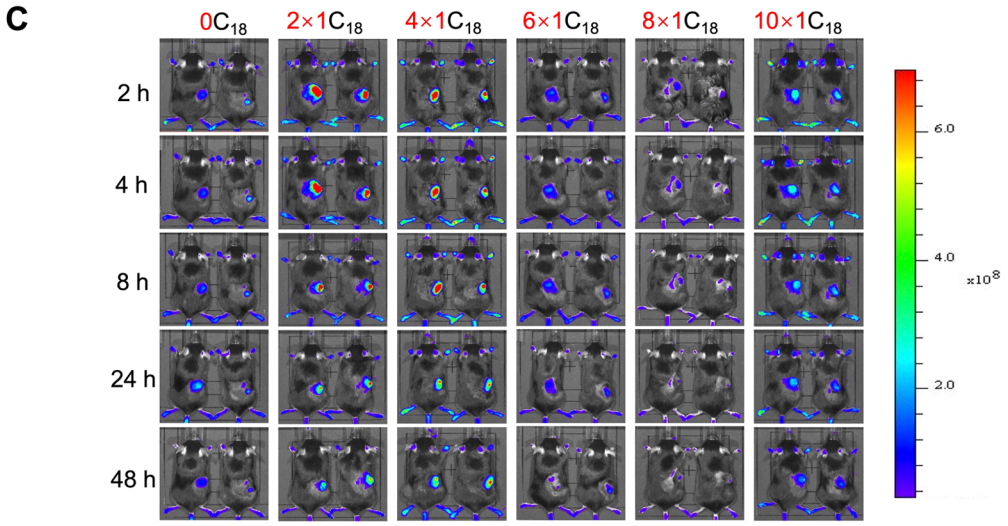

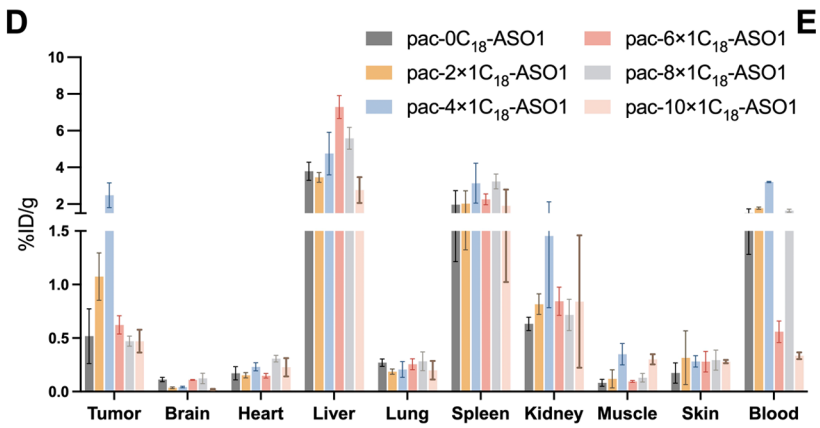

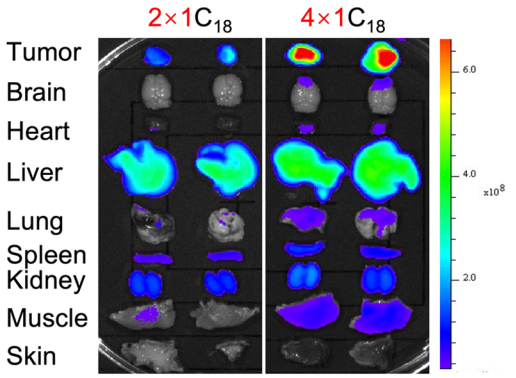

Figure 4. Plasma PK and biodistribution of ribose-based pacDNAs. (A) Plasma PK of Cy5-labeled pacDNA and free DNA in C57BL/6 mice following i.v. injection. Statistical analysis was performed using two-way ANOVA. ****$P < 0.0001$. (B) Plasma PK parameters of ribose-based pacDNAs with variant numbers of the C_{18} modifier. (C) Live animal fluorescence imaging of C57BL/6 mice bearing the K273 allograft following i.v. injection of Cy5-labeled pacDNA. Areas surrounding the allograft have been shaved to facilitate imaging. (D,E) Quantitative biodistribution and *ex vivo* imaging of pacDNAs in major organs/tissues of tumor-bearing C57BL/6 mice 72 h post i.v. injection.

injected dose per gram of tissue (% ID/g, Figure 4D). Again, pacDNAs with two or four R-C_{18} units exhibit stronger tumor localization compared to those with six, eight, or ten C_{18} modifiers. Because pac-4 × 1C_{18} shows the highest tumor distribution compared with other backbone designs (Figures 4E and S6), we focused on this specific arrangement for subsequent studies.

To investigate the antitumor efficacy of pac-4 × 1C_{18} using the K273 allograft model, we prepared pac-4 × 1C_{18}-ASO2, which is matched to the mouse wild-type KRAS mRNA sequence at the 3′ UTR region. First, we validated the potency of pac-4 × 1C_{18}-ASO2 using the K273 cell line *in vitro*. Western blot shows that pac-4 × 1C_{18}-ASO2 downregulated KRAS protein levels in a dose-dependent manner (Figure S7A). The MTT cell viability assay showed that pac-4 × 1C_{18}-ASO2 reduced K273 cell viability, while free ASO2 or pac-4 × 1C_{18}-scramble showed no inhibitory effect (Figure S7B). The antitumor efficacy of pac-4 × 1C_{18}-ASO2 was assessed in female C57BL/6 mice bearing subcutaneous K273 allografts. When the allografts reached a volume of 100 mm^3, 0.5 μmol/

https://doi.org/10.1021/jacs.4c13285
J. Am. Chem. Soc. 2024, 146, 34763−34770

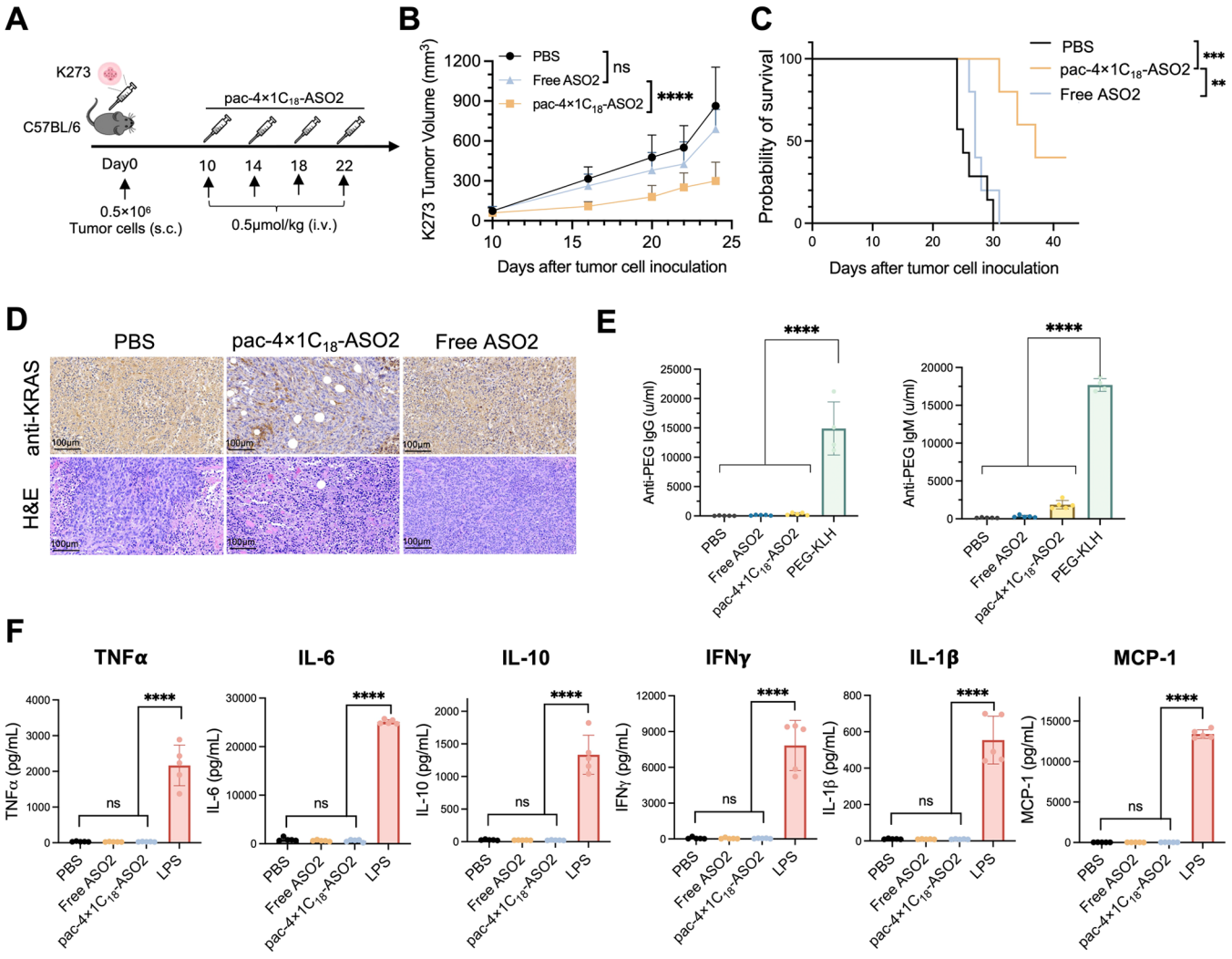

Figure 5. *In vivo* antitumor efficacy of ribose-based pacDNAs. (A) K273 allograft volume changes in 24 days with i.v. injection of PBS, ASO2, and pac-4 × $1C_{18}$-ASO2 at equivalent ASO doses (0.5 μmol/kg) every 4 days since day 10. Injections are indicated by black arrows. (B) Mean tumor growth curve. (C) Kaplan−Meier end point animal survival analysis. Statistical analysis was calculated by the log-rank test. (D) Immunohistostaining and H & E staining of K273 tumor after treatment. (E) Anti-PEG IgM and IgG levels in C57BL/6 mice plasma after i.v. injection of PBS, free ASO2, pac-4 × $1C_{18}$-ASO2, and PEG-KLH (positive control) at 0.5 μmol/kg every 4 days for four doses. Plasma was collected 1 week after the last dose. Statistical analysis was performed using one-way ANOVA. (F) Selected cytokine and chemokine levels in C57BL/6 mice plasma 5 h after i.v. injection of PBS, free ASO2, pac-4 × $1C_{18}$-ASO2 (2 μmol/kg), and LPS (0.5 mg/kg). Statistical analysis was performed using two-way ANOVA (B) and one-way ANOVA (E,F). ****$P < 0.0001$, ***$P < 0.001$, **$P < 0.01$, *$P < 0.05$.

kg of pac-4 × $1C_{18}$-ASO2, free ASO2, or vehicle (PBS) were administrated i.v. once every 4 days for a total of four doses (Figure 5A). By day 24 after tumor inoculation, the average tumor volume of the vehicle group reached 864 mm^3, while pac-4 × $1C_{18}$-ASO2 significantly inhibited tumor growth and extended mice survival with the average tumor volume at 299 mm^3 (Figure 5B,C). In contrast, free ASO2 elicited no survival benefit. Neither pac-4 × $1C_{18}$-ASO2 nor free ASO2 lead to significant body weight changes (Figure S8). Immunohistostaining of tumor tissue revealed reduced KRAS protein expression after pac-4 × $1C_{18}$-ASO2 treatment but not with free ASO2 (Figure 5D).

Next, we performed *in vivo* safety analysis of pac-4 × $1C_{18}$-ASO2. Hematoxylin and eosin (H & E) staining demonstrated no obvious histological changes in major internal organs (Figure S9). Macromolecular therapeutics requiring repeated dosing may induce antidrug adaptive immunity, leading to loss of drug activity in subsequent doses. To evaluate the anti-PEG immunoglobulin IgM/IgG response, healthy C57BL/6 mice were administrated pac-4 × $1C_{18}$-ASO2 or free ASO2 every 4 days for four doses. Mouse plasma was collected 1 week after the last dose. Enzyme-linked immunosorbent assays (ELISA) revealed that pac-4 × $1C_{18}$-ASO2 induced very limited levels of anti-PEG IgM/IgG (Figure 5E). Both responses were minor compared to the positive control (PEG-keyhole limpet hemocyanin [KLH] conjugate). To further investigate possible unintended activation of the immune system, C57BL/6 mouse plasma was collected 3 h after i.v. injection of pac-4 × $1C_{18}$-ASO2 or free ASO2, and cytokines and chemokines related to innate and adaptive immune responses were measured. The assay detected no apparent cytokines or chemokines for either pac-4 × $1C_{18}$-ASO2 or free ASO2 treatment groups, while lipopolysaccharide (LPS) i.v. injection (positive control) generated high levels of cytokines/chemokines (Figure 5F).

https://doi.org/10.1021/jacs.4c13285
J. Am. Chem. Soc. 2024, 146, 34763−34770

CONCLUSIONS

In conclusion, our study presents a robust approach to construct bottlebrush polymers with arbitrary control of the backbone size, composition, and monomer sequence. These capabilities allow us to take advantage of C_{18} modifiers and optimize biological properties such as cell uptake and tumor localization. Experimental and computational studies suggest that the different arrangements of C_{18} affect their self-interaction, which, in turn, modifies their readiness to engage with the cell membrane. Through optimization, we identified pac-4 × $1C_{18}$ as overall the most favorable given *in vitro* cell uptake, gene silencing, and biodistribution in mice. A comparison between pac-4 × $1C_{18}$ and the previously published polynorbornene bottlebrush (pac-PN) indicates that pac-4 × $1C_{18}$ exhibits superior batch-to-batch consistency, improved structural control, and enhanced tumor distribution. In a $KRAS^{G12D}$ lung cancer allograft, a KRAS-depleting pac-4 × $1C_{18}$ showed single-agent tumor-suppressive potency at a fraction of concentration typically used for the ASO modality. Taken together, our results provide valuable insights into the pacDNA structure−property relationship and suggest the possibility of tuning the polymer backbone to meet the delivery requirements of various diseases.

ASSOCIATED CONTENT

Supporting Information

The Supporting Information is available free of charge at https://pubs.acs.org/doi/10.1021/jacs.4c13285.

Materials, experimental procedures and methods, sequences, synthesis, NMR spectroscopy, DLS, dynamic simulation, confocal, *in vitro* assays, and H & E staining of mouse major organs after treatment (PDF)

AUTHOR INFORMATION

Corresponding Author

Ke Zhang − *Department of Chemistry and Chemical Biology, Northeastern University, Boston, Massachusetts 02115, United States; Department of Bioengineering and Department of Chemical Engineering, Northeastern University, Boston, Massachusetts 02115, United States;* orcid.org/0000-0002-8142-6702; Email: k.zhang@northeastern.edu

Authors

Yun Wei − *Department of Chemistry and Chemical Biology, Northeastern University, Boston, Massachusetts 02115, United States*

Peiru Chen − *Department of Chemistry and Chemical Biology, Northeastern University, Boston, Massachusetts 02115, United States*

Mengqi Ren − *Department of Chemistry and Chemical Biology, Northeastern University, Boston, Massachusetts 02115, United States*

Deng Li − *Department of Bioengineering, Northeastern University, Boston, Massachusetts 02115, United States;* orcid.org/0009-0002-3030-8009

Jiachen Lin − *Department of Chemistry and Chemical Biology, Northeastern University, Boston, Massachusetts 02115, United States*

Tingyu Sun − *Department of Chemistry and Chemical Biology, Northeastern University, Boston, Massachusetts 02115, United States*

Yuyan Wang − *Department of Chemistry and Chemical Biology, Northeastern University, Boston, Massachusetts 02115, United States*

Shaobo Yang − *Department of Bioengineering, Northeastern University, Boston, Massachusetts 02115, United States;* orcid.org/0009-0006-5257-6775

Christopher Nenopoulos − *Department of Chemistry and Chemical Biology, Northeastern University, Boston, Massachusetts 02115, United States*

Christopher Oetheimer − *Department of Chemistry and Chemical Biology, Northeastern University, Boston, Massachusetts 02115, United States*

Yao Li − *Department of Bioengineering, Northeastern University, Boston, Massachusetts 02115, United States*

Chenyang Xue − *Department of Chemistry and Chemical Biology, Northeastern University, Boston, Massachusetts 02115, United States*

Mona Minkara − *Department of Bioengineering, Northeastern University, Boston, Massachusetts 02115, United States;* orcid.org/0000-0003-1821-2725

Complete contact information is available at: https://pubs.acs.org/10.1021/jacs.4c13285

Author Contributions

[‖]Y.W., P.C., and M.R. contributed equally. The manuscript was written through contributions of all authors. All authors have given approval to the final version of the manuscript.

Funding

This publication was made possible by the National Science Foundation (DMR award number 2004947), the National Institute of General Medical Sciences (1R01GM121612), and the National Cancer Institute (4R42CA275425 and 5R01CA251730).

Notes

The authors declare the following competing financial interest(s): K.Z. hold financial interest in pacDNA Inc., a company com-mercializing the pacDNA technology.

ACKNOWLEDGMENTS

We gratefully acknowledge Dr. Jean Zhao for gifting the K273 cell line. We are grateful to the Northeastern University-Institutional Animal Care and Use Committee for supporting our animal studies. We thank Dr. Guoxin Rong from the Institute for Chemical Imaging of Living System at Northeastern University for assistance with confocal microscopy. We appreciate Rafay Abu from Barnett Institute of Chemical and Biological Science for HRMS analysis.

REFERENCES

(1) Moumne, L.; Marie, A. C.; Crouvezier, N. Oligonucleotide Therapeutics: From Discovery and Development to Patentability. *Pharmaceutics* **2022**, *14* (2), 260.

(2) Zhang, Q.; Yang, L.; Liu, Y. H.; Wilkinson, J. E.; Krainer, A. R. Antisense oligonucleotide therapy for H3.3K27M diffuse midline glioma. *Sci. Transl. Med.* **2023**, *15*, 691.

(3) Lundin, K. E.; Gissberg, O.; Smith, C. I. E. Oligonucleotide Therapies: The Past and the Present. *Hum. Gene Ther.* **2015**, *26* (8), 475−485.

(4) Lauffer, M. C.; van Roon-Mom, W.; Aartsma-Rus, A.; Collaborative, N. Possibilities and limitations of antisense oligonucleotide therapies for the treatment of monogenic disorders. *Commun. Med-London* **2024**, *4* (1), 6.

(5) Faria, M.; Ulrich, H. The Use of Synthetic Oligonucleotides as Protein Inhibitors and Anticode Drugs in Cancer Therapy: Accomplishments and Limitations. *Curr. Cancer Drug Tar* **2002**, *2* (4), 355−368.
(6) Bost, J. P.; Barriga, H.; Holme, M. N.; Gallud, A.; Maugeri, M.; Gupta, D.; Lehto, T.; Valadi, H.; Esbjorner, E. K.; Stevens, M. M.; et al. Delivery of oligonucleotide therapeutics: Chemical modifications, lipid nanoparticles, and extracellular vesicles. *ACS Nano* **2021**, *15* (9), 13993−14021.
(7) Tan, X.; Jia, F.; Wang, P.; Zhang, K. Nucleic acid-based drug delivery strategies. *J. Controlled Release* **2020**, *323*, 240−252.
(8) Hammond, S. M.; Aartsma-Rus, A.; Alves, S.; Borgos, S. E.; Buijsen, R. A.; Collin, R. W.; Covello, G.; Denti, M. A.; Desviat, L. R.; Echevarría, L.; et al. Delivery of oligonucleotide-based therapeutics: challenges and opportunities. *EMBO Mol. Med.* **2021**, *13* (4), No. e13243.
(9) Chen, P. R.; Wei, Y.; Sun, T. Y.; Lin, J. C.; Zhang, K. Enabling safer, more potent oligonucleotide therapeutics with bottlebrush polymer conjugates. *J. Controlled Release* **2024**, *366*, 44−51.
(10) Khvorova, A.; Watts, J. K. The chemical evolution of oligonucleotide therapies of clinical utility. *Nat. Biotechnol.* **2017**, *35* (3), 238−248.
(11) Roberts, T. C.; Langer, R.; Wood, M. J. A. Advances in oligonucleotide drug delivery. *Nat. Rev. Drug Discov.* **2020**, *19* (10), 673−694.
(12) Lu, X.; Tran, T. H.; Jia, F.; Tan, X.; Davis, S.; Krishnan, S.; Amiji, M. M.; Zhang, K. Providing Oligonucleotides with Steric Selectivity by Brush-Polymer-Assisted Compaction. *J. Am. Chem. Soc.* **2015**, *137* (39), 12466−12469.
(13) Lu, X.; Zhang, K. PEGylation of therapeutic oligonucletides: From linear to highly branched PEG architectures. *Nano Res.* **2018**, *11* (10), 5519−5534.
(14) Jia, F.; Lu, X.; Tan, X.; Wang, D.; Cao, X.; Zhang, K. Effect of PEG Architecture on the Hybridization Thermodynamics and Protein Accessibility of PEGylated Oligonucleotides. *Angew. Chem., Int. Ed. Engl.* **2017**, *56* (5), 1239−1243.
(15) Wang, D.; Lin, J.; Jia, F.; Tan, X.; Wang, Y.; Sun, X.; Cao, X.; Che, F.; Lu, H.; Gao, X.; et al. Bottlebrush-architectured poly (ethylene glycol) as an efficient vector for RNA interference in vivo. *Sci. Adv.* **2019**, *5* (2), No. eaav9322.
(16) Wang, D.; Wang, Q.; Wang, Y.; Chen, P.; Lu, X.; Jia, F.; Sun, Y.; Sun, T.; Zhang, L.; Che, F.; et al. Targeting oncogenic KRAS with molecular brush-conjugated antisense oligonucleotides. *Proc. Natl. Acad. Sci. U.S.A.* **2022**, *119* (29), No. e2113180119.
(17) Ross, S. J.; Revenko, A. S.; Hanson, L. L.; Ellston, R.; Staniszewska, A.; Whalley, N.; Pandey, S. K.; Revill, M.; Rooney, C.; Buckett, L. K.; et al. Targeting KRAS-dependent tumors with AZD4785, a high-affinity therapeutic antisense oligonucleotide inhibitor of KRAS. *Sci. Transl. Med.* **2017**, *9* (394), No. eaal5253.
(18) McCormick, F. KRAS as a therapeutic target. *Clin. Cancer Res.* **2015**, *21* (8), 1797−1801.
(19) Wang, Y.; Wang, D.; Lin, J.; Lyu, Z.; Chen, P.; Sun, T.; Xue, C.; Mojtabavi, M.; Vedadghavami, A.; Zhang, Z.; et al. A Long-Circulating Vector for Aptamers Based upon Polyphosphodiester-Backboned Molecular Brushes. *Angew. Chem., Int. Ed. Engl.* **2022**, *61* (41), No. e202204576.
(20) Juliano, R. L. The delivery of therapeutic oligonucleotides. *Nucleic Acids Res.* **2016**, *44*, 6518−6548.
(21) Karaki, S.; Benizri, S.; Mejias, R.; Baylot, V.; Branger, N.; Nguyen, T.; Vialet, B.; Oumzil, K.; Barthelemy, P.; Rocchi, P. Lipid-oligonucleotide conjugates improve cellular uptake and efficiency of TCTP-antisense in castration-resistant prostate cancer. *J. Controlled Release* **2017**, *258*, 1−9.
(22) Chen, Y.; Wang, S.; Ma, Q.; Wu, X.; Guo, Q.; Luo, X.; Tao, L.; Shen, X. Utilizing endosomal capture for tumor therapy via membrane-lytic mechanism-based Pickering emulsion. *J. Controlled Release* **2023**, *354*, 523−537.
(23) Lee, Y.; Thompson, D. H. Stimuli-responsive liposomes for drug delivery. *Wiley Interdiscip. Rev. Nanomed. Nanobiotechnol.* **2017**, *9*, No. e1450.

https://doi.org/10.1021/jacs.4c13285
J. Am. Chem. Soc. 2024, 146, 34763−34770